



HAL
open science

The oxidation state of iron in Mid-Ocean Ridge basalt glasses by Raman spectroscopy

Charles Le Losq, Andrew J Berry, Mark A Kendrick, Daniel R. Neuville,
Hugh St. C O'Neill

► **To cite this version:**

Charles Le Losq, Andrew J Berry, Mark A Kendrick, Daniel R. Neuville, Hugh St. C O'Neill. The oxidation state of iron in Mid-Ocean Ridge basalt glasses by Raman spectroscopy. *The American Mineralogist*, 2019, 104 (7), pp.1032-1042. 10.2138/am-2019-6887 . hal-02989700

HAL Id: hal-02989700

<https://hal.science/hal-02989700v1>

Submitted on 12 Nov 2020

HAL is a multi-disciplinary open access archive for the deposit and dissemination of scientific research documents, whether they are published or not. The documents may come from teaching and research institutions in France or abroad, or from public or private research centers.

L'archive ouverte pluridisciplinaire **HAL**, est destinée au dépôt et à la diffusion de documents scientifiques de niveau recherche, publiés ou non, émanant des établissements d'enseignement et de recherche français ou étrangers, des laboratoires publics ou privés.

1. Introduction

Mid-Ocean Ridge Basalts (MORB), derived from partial melting of the upper mantle, are of critical importance for understanding the geochemistry of the mantle and the formation of the oceanic crust (e.g. Langmuir et al., 1992; Asimow et al., 2004; Gale et al., 2013; O'Neill et al., 2018). MORB glasses, formed by rapid cooling at the rim of pillow lavas enable the composition (Jenner and O'Neill, 2012; O'Neill and Jenner, 2012), including volatile content (Kendrick et al., 2013), and oxidation state (Christie et al., 1986; Bézou and Humler, 2005; Cottrell and Kelley, 2011, 2013; Berry et al., 2018; Zhang et al., 2018) of the melts to be determined. This, in turn, allows the intensive and extensive thermodynamic conditions of the mantle source to be calculated (e.g. Asimow et al., 2004). In particular, the iron oxidation state of Fe in MORB, expressed as $\text{Fe}^{3+}/\text{Fe}^{\text{TOT}}$ with $\text{Fe}^{\text{TOT}} = \text{Fe}^{2+} + \text{Fe}^{3+}$, is important because it affects estimations of temperature, mineral assemblages, and the speciation of volatile elements, at both the surface and magmatic source.

The latest average $\text{Fe}^{3+}/\text{Fe}^{\text{TOT}}$ values of natural MORB glasses from global sources have been determined to be 0.10 ± 0.02 (Berry et al., 2018) or 0.14 ± 0.01 (Zhang et al., 2018) by Fe K-edge XANES spectroscopy, and 0.11 ± 0.02 by wet-chemistry (corrected for plagioclase phenocrysts, Bézou and Humler, 2005). Wet chemistry is a destructive method that lacks spatial resolution and is unsuitable for inhomogeneous glasses or small samples such as melt inclusions (e.g. see Bézou and Humler, 2005). Fe K-edge XANES spectroscopy has excellent precision and micron spatial resolution in two dimensions, but requires standards that are compositionally matched and for which $\text{Fe}^{3+}/\text{Fe}^{\text{TOT}}$ is determined by another technique, such as ^{57}Fe Mössbauer spectroscopy (e.g. Berry et al., 2008). There are also questions concerning possible photo-oxidation during analysis of hydrous glasses (e.g. Cottrell et al., in press). A considerable drawback is that it also requires access to a synchrotron light source.

Raman spectroscopy is an alternative technique for determining $\text{Fe}^{3+}/\text{Fe}^{\text{TOT}}$ that is easily accessible for most investigators, is non-destructive, has micron-scale spatial resolution, requires minimal sample preparation, is easy to perform, and spectra can be acquired within minutes. Previous studies have shown how Raman spectroscopy can be used for quantifying the concentration of H_2O (Thomas, 2000; Zajacz et al., 2005; Behrens et al., 2006; Thomas et al., 2008; Mercier et al., 2009, 2010; Le Losq et al., 2012) and CO_2 (Morizet et al., 2013) in glasses, with applications to pumices and melt inclusions (Shea et al., 2014; Métrich et al.,

69 2016). The potential of Raman spectroscopy to determine $\text{Fe}^{3+}/\text{Fe}^{\text{TOT}}$ in glasses has been
70 demonstrated previously using various data treatment protocols (Magnien et al., 2004, 2006,
71 2008; Roskosz et al., 2008; Di Muro et al., 2009; Di Genova et al., 2016). The simplest
72 method requires correlating changes in $\text{Fe}^{3+}/\text{Fe}^{\text{TOT}}$ with changes in the intensity of the Raman
73 spectra at given Raman shift (Magnien et al., 2006; Roskosz et al., 2008). A more complex
74 method involves peak fitting the Raman signals assigned to stretching of tetrahedral SiO_4 and
75 AlO_4 units in order to extract the Fe^{3+} -O signal, which can be related to $\text{Fe}^{3+}/\text{Fe}^{\text{TOT}}$ (Di Muro
76 et al., 2009; Welsch et al., 2017). Recently, Di Genova et al. (2016) proposed another
77 approach based on interpolation between two endmember spectra (e.g., one from a glass with
78 oxidized iron and one from a glass with the same composition but reduced iron). Those
79 different studies focused on demonstrating the ability of Raman spectroscopy to quantify
80 $\text{Fe}^{3+}/\text{Fe}^{\text{TOT}}$ in glasses of known composition. To date, no systematic use of Raman
81 spectroscopy has been attempted to tackle a problem such as the quantification of $\text{Fe}^{3+}/\text{Fe}^{\text{TOT}}$
82 in MORB glasses.

83

84 The existing methods for quantifying $\text{Fe}^{3+}/\text{Fe}^{\text{TOT}}$ of glasses from Raman spectra rely on either
85 simple treatments (e.g. the intensity of one or several peaks, mixing end-member spectra) or
86 peak fitting. To our knowledge, machine learning algorithms, which remove subjectivity in
87 the data reduction protocol, have not been used for determining $\text{Fe}^{3+}/\text{Fe}^{\text{TOT}}$ of glasses. Here
88 we compare existing data reduction methods (*conventional methods*), based on spectral
89 intensity variations and mixing of spectra, with new supervised and unsupervised machine
90 learning approaches. We avoided the peak fitting procedure (e.g. Di Muro et al., 2009)
91 because it is complex to perform and equivocal of interpretation (Welsch et al., 2017), and
92 thus may not be suited to a routine protocol. Conventional methods and supervised machine
93 learning require the $\text{Fe}^{3+}/\text{Fe}^{\text{TOT}}$ values of the glass standards to be known. Unsupervised
94 machine learning methods, however, do not require prior knowledge of $\text{Fe}^{3+}/\text{Fe}^{\text{TOT}}$ of the
95 standards, such that they offer an independent way of determining $\text{Fe}^{3+}/\text{Fe}^{\text{TOT}}$ for comparison
96 with the results of other techniques. Those methods were assessed for a set of 13 synthetic
97 glasses with a typical but simplified MORB composition and known $\text{Fe}^{3+}/\text{Fe}^{\text{TOT}}$ (Berry et al.,
98 2018). Following the proof of concept, the methods were used to determine $\text{Fe}^{3+}/\text{Fe}^{\text{TOT}}$ of a
99 representative set of 42 natural MORB glasses from the Atlantic, Indian and Pacific oceans,
100 with known major and trace elements compositions (Melson et al., 2002; Jenner and O'Neill,
101 2012; Kendrick et al., 2013) and Fe K-edge XANES $\text{Fe}^{3+}/\text{Fe}^{\text{TOT}}$ values (Berry et al., 2018).

102

103

104 **2. Material and Methods**

105

106 *2.1 Starting Glasses*

107

108 The MORB standards were prepared from mixtures of reagent grade SiO₂ (52.0 wt%), Al₂O₃
109 (16.1 wt%), CaCO₃ = CaO (12.4 wt%), Fe₂O₃ = FeO (10.0 wt%), MgO (8.2 wt%) and TiO₂
110 (1.3 wt%) that were equilibrated at 1400 °C and values of log *f*O₂ between 0 and -11 (-4.7
111 and 6.3 in log units relative to the quartz-fayalite-magnetite, QFM, buffer) for ~ 24 h before
112 quenching in water. A sample was also prepared at log *f*O₂ = 4.8 (QFM + 11.2) using a piston-
113 cylinder apparatus. The Fe³⁺/Fe^{TOT} ratio of each glass was determined by Mössbauer
114 spectroscopy, and found to vary from ~ 0 to 1 (Table 1). For further details see Berry et al.
115 (2018).

116

117 Samples of natural MORB glass were obtained from the Department of Mineral Sciences,
118 Smithsonian Institution, as polished chips mounted in epoxy resin and are listed by MNNH
119 catalogue numbers in Supplementary Table 1. The sample details and major element
120 composition are given in Melson et al. (2002), their trace element composition in Jenner and
121 O'Neill (2012), and their Fe³⁺/Fe^{TOT} values determined by Fe K-edge XANES spectroscopy
122 in Berry et al. (2018). From the set analysed by Berry et al. (2018), the Raman spectra of five
123 glasses (NMNH No. 111235-85, 115083-41, 113828-5, 111241-1, 111237-67) were
124 contaminated by contributions from crystals (see supplementary code) and were not
125 considered during the data reduction. Five samples previously studied by Kendrick et al.
126 (2013) from Juan de Fuca (Alv 2262-8 and Alv 2269-2), the East Pacific Rise Clipperton (CL
127 DR01) and Mid-Atlantic Ridge MAPCO (CH98 DR08 and CH98 DR11) were also analysed.

128

129 *2.2 Raman Spectra Acquisition*

130

131 Raman spectra of glasses were recorded using a Renishaw InVia spectrometer, equipped with
132 a Peltier-cooled detector, a 2400 l/mm grating and a confocal system. Samples were excited
133 using a 532 nm laser line focused ~ 3 µm below the surface using a x100 Leica objective.
134 The laser power on the sample was ~ 1.2 mW. The spatial resolution was < 1 µm, and the
135 spectral resolution ~ 1.2 cm⁻¹. Five spectra were recorded from different points for each

136 sample. They are treated separately during the data reduction process. The acquisition time
137 varied between 120 and 180 s. For water-bearing natural MORB samples, oxidation of Fe by
138 the laser has been reported at high laser power (Di Genova et al., 2017). The combination of
139 a laser power less than 5 mW (Di Genova et al., 2017) with a relatively short counting time
140 of 120 s, and the analysis of five different spots, was used to prevent Fe oxidation during
141 spectral acquisition. We checked this by recording Raman maps for six samples, by acquiring
142 120 spectra with an acquisition time of 1 s over an area of 10 μm by 12 μm . During the
143 acquisition of these maps, the sample was continuously moved, such that the beam spent less
144 than 1 s at a given location. The individual spectra were noisy, but their average produced a
145 spectrum with a signal to noise ratio similar to that of a spectrum acquired in 120 s at a single
146 point. No difference was observed between spectra obtained in these two ways, indicating
147 that no variation of $\text{Fe}^{3+}/\text{Fe}^{\text{TOT}}$ was induced during acquisition.

148

149 *2.3 Data pre-processing*

150

151 The spectra (Fig. 1) were pre-processed in Python using the Rumpy library (Le Losq, 2018).
152 The data were corrected for temperature and excitation line effects following Galeener and
153 Sen (1978). We focus the data reduction methods on the 800-1300 cm^{-1} region of the spectra,
154 which contains signals from Si-O, Al-O and Fe^{3+} -O stretching in the glass structure (Brawer
155 and White, 1975, 1977; Virgo et al., 1980; Mysen et al., 1982; Virgo et al., 1982). This
156 region also avoided signals due to nanolites ($< 800 \text{ cm}^{-1}$), which were observed in the spectra
157 of some of the natural glasses (see supplementary materials). We chose to fit a linear baseline
158 to subtract the background (Fig. 2A), with the aim of having only Si-O, Al-O and Fe^{3+} -O
159 stretching signals in the background-corrected spectra that will be used for $\text{Fe}^{3+}/\text{Fe}^{\text{TOT}}$
160 determination. The low and high frequency anchors of the linear baseline were determined
161 using a grid-search algorithm as those resulting in the lowest root mean square error (RMSE)
162 between the Mössbauer $\text{Fe}^{3+}/\text{Fe}^{\text{TOT}}$ values and those predicted by the *intensity* and *mixing*
163 methods described in sections 2.4.1 and 2.4.2. This resulted in the subtraction of a linear
164 baseline interpolated between the intensities at 850 and 1140 cm^{-1} (Fig. 2A). The baseline
165 corrected spectra were smoothed using a Whittaker function to maximize the signal to noise
166 ratio (Eilers, 2003; see supplementary code for an example), and then the intensity
167 normalised to vary between 0 and 1 (Fig 2B). The spectra resulting from this arbitrary
168 baseline correction can not be used to infer the glass structure. However, the correction

169 provides a simple method for isolating variations in the Raman signals related to changes in
170 Fe oxidation state (Fig 2B). Furthermore, the arbitrary baseline correction was found to be
171 beneficial because it avoids the introduction of random errors associated with variations in
172 the real spectral background when the sample signal is low (e.g. near 1250 cm⁻¹).

173

174 *2.4 Determining the oxidation state of iron by Raman spectroscopy*

175

176 In this study, six different methods were evaluated to determine the oxidation state of Fe in
177 the suite of MORB glass standards (Table 1) from the background subtracted 850-1140 cm⁻¹
178 region of the Raman spectra (Fig. 2B). The idea is to relate, for a set of glass standards with
179 fixed major element composition, changes in the Raman spectra to changes in Fe³⁺/Fe^{TOT}.
180 The six methods investigated are described below.

181

182 *2.4.1 Intensity method*

183

184 The intensity of the Raman spectra between 850 and 1140 cm⁻¹ varies systematically with
185 Fe³⁺/Fe^{TOT} in the glass standards (Figs. 1, 2B). In particular, the intensity at 930 cm⁻¹ varies
186 strongly with Fe³⁺/Fe^{TOT}. This feature has contributions from Fe³⁺-O (Virgo et al., 1982;
187 Magnien et al., 2006; Di Muro et al., 2009), and thus should be ideal for determining
188 Fe³⁺/Fe^{TOT}. Two methods were tested to quantify the intensity at 930 cm⁻¹: direct
189 measurement at fixed frequency (the average of values between 929 and 931 cm⁻¹) and by
190 peak fitting the 850-1140 cm⁻¹ spectral envelop with arbitrary Gaussian components. Direct
191 measurements of the intensity at 930 cm⁻¹ (hereafter abbreviated I₉₃₀) provided the better
192 precision and this approach was used.

193

194 *2.4.2 Mixing method*

195

196 The *Mixing* method is based on the bilinear model that describes the matrix dataset $D_{n,m}$, of
197 dimension n spectra times m features (i.e. Raman shifts), as:

198

$$199 D_{n,m} = F_{n,k} \cdot S_{k,m} + \varepsilon_{n,m}, \quad (1)$$

200

201 where $F_{n,k}$ is the matrix of component fractions, $S_{k,m}$ the matrix of partial spectral
202 components (endmember spectra), k the number of components and $\varepsilon_{n,m}$ a noise term. In the
203 present case, $k = 2$ (reduced and oxidised endmembers), as verified by a principal component
204 analysis of the 13 standards, which revealed that two components account for more than
205 99.8% of the variance in the data. Using the notation S_{OX} and S_{RED} to designate the oxidised
206 ($\text{Fe}^{3+}/\text{Fe}^{\text{TOT}} = 1$) and reduced ($\text{Fe}^{3+}/\text{Fe}^{\text{TOT}} = 0$) Raman spectral components, and F_{OX} as the
207 fraction of S_{OX} , eq. (1) can be re-arrange as:

208

$$209 \quad D_{n,m} = F_{\text{OX}} \cdot S_{\text{OX}} + (1 - F_{\text{OX}}) \cdot S_{\text{RED}} . \quad (2)$$

210

211 We used least absolute regression (LAD) to determine F_{OX} , because LAD is more robust than
212 least squares with respect to outliers or non-Gaussian distributions (Tarantola, 2005). The
213 optimised F_{OX} values can then be related to the glass $\text{Fe}^{3+}/\text{Fe}^{\text{TOT}}$ values (Di Genova et al.,
214 2016).

215

216 *2.4.3 Alternative Least Square Multivariate Curve Resolution (ALS MCR)*

217

218 Solving eq. (1) usually requires either $F_{n,k}$ or $S_{k,m}$. For example, $F_{n,k}$ are obtained from $S_{k,m}$
219 in the *Mixing* method (sec. 2.4.2). However, several techniques allow both $F_{n,k}$ and $S_{k,m}$ to
220 be estimated from $D_{n,m}$, as for example independent component analysis (e.g. Hyvärinen et
221 al., 2001), non-negative matrix factorisation (e.g. Lin, 2007), and iterative optimisation (e.g.
222 Zakaznova-Herzog et al., 2007). For the present dataset of spectra, several conditions need to
223 be satisfied: (i) $F_{n,k} \in [0,1]$; (ii) $F_{n,1} = 1 - F_{n,2}$; and (iii) $S_{k,m} \in \mathbb{R}^+$. Of the available
224 methods, self-modelling curve resolution (Jiang et al., 2004; de Juan and Tauler, 2006), also
225 known as multivariate curve resolution, can help solve the present problem. As they do not
226 require prior knowledge of neither $F_{n,k}$ nor $S_{k,m}$, those methods belong to the class of
227 unsupervised machine learning algorithms.

228

229 In this study, the *Alternative Least Square Multivariate Curve Resolution (ALS MCR)* method
230 was used to iteratively optimise $F_{n,k}$ and $S_{k,m}$. The PyMCR python library was used, starting
231 the algorithm with estimations of $S_{k,m}$ obtained from mean spectra from our spectral dataset.
232 The algorithm was allowed to perform 50 iterations. After convergence, usually achieved in
233 only a few iterations, optimised $F_{n,k}$ and $S_{k,m}$ matrices are available for the investigated

234 dataset. The spectral endmembers stored in the optimised $S_{k,m}$ matrix (i.e. optimised F_{OX} and
235 F_{RED}) can then be used with the *Mixing* method for new samples.

236

237 Convergence of the *ALS MCR* algorithm is inherently dependent on the starting conditions
238 (e.g. Valderrama et al., 2016). The effects of the range of Fe^{3+}/Fe^{TOT} values included in $D_{n,m}$,
239 and the starting $S_{k,m}$ components, were tested using iterative protocols. The Fe^{3+}/Fe^{TOT}
240 dataset range can be represented by two variables: (i) $\Delta Fe^{3+}/Fe^{TOT}$ of $D_{n,m}$, which represents
241 the difference of Fe^{3+}/Fe^{TOT} between the most reduced and the most oxidized samples in the
242 dataset; and (ii) mean Fe^{3+}/Fe^{TOT} of $D_{n,m}$, which is the mean value of Fe^{3+}/Fe^{TOT} of the
243 dataset.

244 Similarly, variations in the initial $S_{k,m}$ components are represented using two parameters: (i)
245 $\Delta Fe^{3+}/Fe^{TOT}$ of $S_{k,m}$ represents the difference of Fe^{3+}/Fe^{TOT} between the two initial $S_{k,m}$
246 components; and (ii) mean Fe^{3+}/Fe^{TOT} of $S_{k,m}$, which is the average value of the Fe^{3+}/Fe^{TOT} of
247 the two initial $S_{k,m}$ components.

248 To determine how the root-mean-square deviations between the estimated and nominal
249 Fe^{3+}/Fe^{TOT} values of the standard vary with $\Delta Fe^{3+}/Fe^{TOT}$ and mean Fe^{3+}/Fe^{TOT} of $D_{n,m}$, and
250 $\Delta Fe^{3+}/Fe^{TOT}$ and mean Fe^{3+}/Fe^{TOT} of $S_{k,m}$, these values were varied by iteration, such that
251 different subsets of $D_{n,m}$ and $S_{k,m}$ were generated. These subsets were provided to the *ALS*
252 *MCR* algorithm to calculate optimised $S_{k,m}$ and $D_{n,m}$ matrices. These optimised matrices
253 were then used to determine Fe^{3+}/Fe^{TOT} for the entire $D_{n,m}$ and $S_{k,m}$ datasets.

254

255 *2.4.4 Neural Networks, Kernel Ridge and Support Vector regressions*

256

257 The three other techniques that were investigated used the supervised machine learning
258 regression algorithms *Neural Networks*, *Kernel Ridge*, and *Support Vector* from the Scikit
259 Learn library (Pedregosa et al., 2011). An interface for using these algorithms for Raman data
260 was implemented in the Rampy library (Le Losq, 2018) through the class *mlregressor* (see
261 the Jupyter notebook in the supplementary materials as well as the *rampy.mlregressor* help).
262 The machine learning algorithms require the data to be divided into two subsets: a *training*
263 *subset* to train the different algorithms, and a *testing subset* that are treated as unknowns to
264 evaluate the predictive error of the algorithms. The train-test split was performed by

265 randomly sorting the dataset according to their $\text{Fe}^{3+}/\text{Fe}^{\text{TOT}}$ values (function *chemical_splitting*
266 from the rampy library). The testing data subset was ~ 38 % of the total dataset.

267

268 The *Neural Network* technique uses a network of activation units, which are Rectifier
269 functions [$y = \max(0,x)$] (Glorot et al., 2011) in the present study, to map the relationship
270 between the Raman spectra and $\text{Fe}^{3+}/\text{Fe}^{\text{TOT}}$ values of the glasses (see description in Bengio,
271 2009 and references therein). The activation units have adjustable parameters, called weights
272 and bias, that are optimised by least square regression. This method makes no assumptions
273 about the linearity of variations in the Raman spectra with $\text{Fe}^{3+}/\text{Fe}^{\text{TOT}}$. The network was
274 optimised by testing different architectures to minimize the training and testing errors, and to
275 keep those two values as close as possible to each other. A simple architecture with three
276 activation units in a single hidden layer provided the most robust fits. Adding more
277 activations units or layers did not decrease the error metrics of the network, and hence this
278 simple architecture was used. The Limited-memory Broyden-Fletcher-Goldfarb-Shanno
279 (*lbfgs*) solver was chosen, as it performs better than others for the present small dataset.
280 Bagging, which consists of training multiple networks and returning the average of their
281 outputs (Breiman and Breiman, 1996), was performed to avoid over-fitting and to promote
282 the ability of the network to predict new values. A total of 100 networks were trained, and the
283 results represent the average output of these 100 networks.

284

285 The *Kernel Ridge* and *Support Vector* techniques regress the data after their projection in a
286 high-dimensionality space. This projection was done using a non-linear radial basis kernel
287 function, such that the Raman intensity can non-linearly depend on $\text{Fe}^{3+}/\text{Fe}^{\text{TOT}}$. The
288 difference between the *Kernel Ridge* and *Support Vector* regressions lies in the use of
289 different loss functions: *Kernel Ridge* regression uses a penalized (l_2 normalisation) residual
290 of the sum of squares, whereas *Support Vector* regression uses a ϵ -insensitive loss function (ϵ
291 is a deviation term in the loss function, i.e. the predictions are allowed to be as far from the
292 calibration data as ϵ). More information on these algorithms is available in Murphy (2012),
293 Smola and Schölkopf (2004) and Vapnik (1999). The hyper-parameters of the *Kernel Ridge*
294 and *Support Vector* algorithms were automatically tuned by performing a random 5-fold
295 cross-validation on the training dataset.

296

297 A Jupyter notebook running under the Python language, together with all the spectra, are
298 provided as supplementary materials to enable the results of this study, and the figures, to be
299 reproduced.

300

301

302

303 **3. Results**

304

305 *3.1 Raman spectra of MORB glass standards*

306

307 The Raman spectra of the MORB glass standards exhibit peaks and shoulders at ~ 505, 570,
308 660, 735, 804, 930 and 1005 cm⁻¹ (A to G markers in Fig. 1), with intensities that depend on
309 Fe³⁺/Fe^{TOT}. The intensity of the A, B, C and D Raman signals decreases with decreasing
310 Fe³⁺/Fe^{TOT} (Fig. 1, Table 1), whereas that of E and G increases (Figs. 1, 2B). The intensity of
311 F relative to that of G decreases with decreasing Fe³⁺/Fe^{TOT} (Fig. 2B).

312

313 The changes in the Raman spectra of the glasses following changes in Fe³⁺/Fe^{TOT} reflect
314 changes in (i) the Fe³⁺ contribution to the Raman signals, and (ii) the overall glass structure
315 as Fe³⁺ and Fe²⁺ have different roles. The signals in the 810-1300 cm⁻¹ region of the Raman
316 spectra of MORB glasses can be assigned to symmetric and asymmetric stretching of Qⁿ
317 SiO₄-AlO₄ units, where *n* is the number of bridging oxygens (Brawer and White, 1975, 1977;
318 Furukawa and White, 1980; Furukawa et al., 1981; Mysen et al., 1982; McMillan, 1984;
319 Mysen, 1990; Le Losq and Neuville, 2013; Le Losq et al., 2014). The intensity at F is
320 assigned to the combination of signals from Fe³⁺-O stretching in the glass network (Virgo et
321 al., 1982; Wang et al., 1995; Magnien et al., 2004, 2006, 2008; Di Muro et al., 2009; Cochain
322 et al., 2012) and Si-O stretching in Q² units (McMillan, 1984; Mysen et al., 1982; Virgo et
323 al., 1980). This assignment agrees with (i) the decrease in the relative intensity of F with Fe
324 reduction (Figs. 1, 2B) and (ii) the presence of F as a shoulder in the most reduced spectra
325 (Figs. 1, 2B). The peak near 1005 cm⁻¹ mainly comprises contributions from Si-O and Al-O
326 stretching in Q³ units. This signal usually occurs near 1100 cm⁻¹ in Al-free silicate glasses
327 (e.g. Mysen et al., 1982; McMillan, 1984) but shifts to lower frequencies in aluminosilicate
328 glasses (Neuville and Mysen, 1996; Mysen et al., 2003; Le Losq and Neuville, 2013). This
329 assignment is consistent with the composition of MORB glasses; with NBO/T values ranging

330 from ~ 0.5 to ~ 1.0 (Mysen and Richet, 2005), they are expected to be enriched in Q^3 units
331 and to contain minor fractions of Q^2 and Q^4 (e.g. Maekawa et al., 1991).

332

333 *3.2 Raman spectroscopy as a tool for determining Fe^{3+}/Fe^{TOT} of MORB glasses*

334

335 *3.2.1 The Intensity method*

336

337 I_{930} in the Raman spectra of the synthetic MORB glasses is linearly correlated with
338 Fe^{3+}/Fe^{TOT} (Fig. 3), with a correlation coefficient of 0.9973. It is thus possible to determine
339 Fe^{3+}/Fe^{TOT} of a glass from the I_{930} scaled Raman intensity using the equation:

340

$$341 \quad Fe^{3+}/Fe^{TOT} = 4.084(38) \times I_{930} - 2.779(29) . \quad (3)$$

342

343 The root-mean-square deviation between the Fe^{3+}/Fe^{TOT} values of the standards and those
344 calculated with eq. 3 is 0.02 (1σ).

345

346 *3.2.2 The Mixing method*

347

348 Following a protocol similar to that described by Di Genova et al. (2016), we used the
349 average of the five spectra recorded for the most oxidized and reduced glasses ($\log fO_2 = 4.8$
350 and -11.0 , Table 1) as endmembers. Then, F_{OX} was adjusted by least absolute regression to
351 obtain mixed spectra that matched the observed ones (Fig. 4A). The correlation between F_{OX}
352 and Fe^{3+}/Fe^{TOT} is shown in Figure 4B; the correlation coefficient is 0.9974. F_{OX} is linearly
353 proportional to Fe^{3+}/Fe^{TOT} . This result differs from the finding of Di Genova et al. (2016),
354 who reported non-linear variations of F_{OX} with Fe^{3+}/Fe^{TOT} for rhyolite and basalt glasses.
355 This may be due to the fact that these authors did not use endmember spectra with Fe^{3+}/Fe^{TOT}
356 of 0 and 1, but of intermediate values. In the present case, F_{OX} and Fe^{3+}/Fe^{TOT} are related by:

357

$$358 \quad Fe^{3+}/Fe^{TOT} = 1.02(1) \times F_{OX} - 0.003(4) . \quad (4)$$

359

360 F_{OX} directly gives Fe^{3+}/Fe^{TOT} of MORB glasses to within 0.03 (1σ).

361

362 *3.2.3 The ALS MCR method*

363

364 For a set of glasses with unknown but varying $\text{Fe}^{3+}/\text{Fe}^{\text{TOT}}$ values, *ALS MCR* can determine
365 the endmember spectra (i.e. spectra corresponding to $\text{Fe}^{3+}/\text{Fe}^{\text{TOT}} = 0$ and 1), and hence,
366 $\text{Fe}^{3+}/\text{Fe}^{\text{TOT}}$ for any MORB glass by linear combination fitting.

367

368 Figure 5 presents the results obtained from tests performed to evaluate the sensitivity of *ALS*
369 *MCR* to the starting conditions (see sec. 2.4.3). The best results were obtained when the
370 dataset covered the widest possible range of $\text{Fe}^{3+}/\text{Fe}^{\text{TOT}}$ values, i.e. when $\Delta \text{Fe}^{3+}/\text{Fe}^{\text{TOT}}$ of
371 $D_{n,m} \rightarrow 1$ and mean $\text{Fe}^{3+}/\text{Fe}^{\text{TOT}}$ of $D_{n,m} \rightarrow \sim 0.4 - 0.5$ (Fig. 5A). $\text{Fe}^{3+}/\text{Fe}^{\text{TOT}}$ root-mean-square
372 deviations < 0.06 were achieved using datasets with $\Delta \text{Fe}^{3+}/\text{Fe}^{\text{TOT}}$ of $D \geq 0.75$ and mean
373 $\text{Fe}^{3+}/\text{Fe}^{\text{TOT}}$ of $D \in [0.35, 0.55]$. The choice of the initial $S_{k,m}$ seems less critical, but still
374 affects the accuracy of the *ALS MCR* method (Fig. 5B). $\text{Fe}^{3+}/\text{Fe}^{\text{TOT}}$ root-mean-square
375 deviations < 0.03 were obtained for initial $S_{k,m}$ with mean $\text{Fe}^{3+}/\text{Fe}^{\text{TOT}} \in [0.4, 0.6]$ and Δ
376 $\text{Fe}^{3+}/\text{Fe}^{\text{TOT}} \in [0.1, 0.6]$.

377

378 The *ALS MCR* method was tested further by optimising $S_{k,m}$ using the full dataset $D_{n,m}$.
379 From Figure 5B, initial S components with $\Delta \text{Fe}^{3+}/\text{Fe}^{\text{TOT}}$ and mean $\text{Fe}^{3+}/\text{Fe}^{\text{TOT}}$ of ~ 0.5 and
380 0.4 , respectively, should provide best results. Thus, the mean spectra at $\text{Fe}^{3+}/\text{Fe}^{\text{TOT}} = 0.66$ and
381 0.25 were selected as initial $S_{k,m}$ components. Selecting mean spectra with $\text{Fe}^{3+}/\text{Fe}^{\text{TOT}} = 0$
382 and 1 does not significantly change the results, but the present choice allows the effects of
383 differences in the initial and optimised $S_{k,m}$ components to be illustrated, as shown in Figure
384 6A. The optimised $S_{k,m}$ spectra are clearly different from their initial values, demonstrating
385 the ability of *ALS MCR* to identify the true $S_{k,m}$ endmembers. The optimised $S_{k,m}$ produce
386 good fits to the observed spectra (Fig. 6B). The fraction of the oxidised endmember, C_{OX} , is
387 linearly related to the $\text{Fe}^{3+}/\text{Fe}^{\text{TOT}}$ of the glass by (Fig. 6C):

388

$$389 \text{Fe}^{3+}/\text{Fe}^{\text{TOT}} = 1.07(1) \times C_{\text{OX}} - 0.035(5) . \quad (5)$$

390

391 Contrary to F_{OX} , C_{OX} is not directly equal to $\text{Fe}^{3+}/\text{Fe}^{\text{TOT}}$. This is because of small differences
392 between the optimised $S_{k,m}$ endmembers and the mean Raman spectra at $\text{Fe}^{3+}/\text{Fe}^{\text{TOT}} = 0$ and
393 1 (residuals shown in Fig. 6A). These differences introduce a bias, such that using C_{OX} as a
394 direct estimate of $\text{Fe}^{3+}/\text{Fe}^{\text{TOT}}$ leads to slightly (~ 0.02) under- and over-estimations of
395 $\text{Fe}^{3+}/\text{Fe}^{\text{TOT}}$, depending on the glass $\text{Fe}^{3+}/\text{Fe}^{\text{TOT}}$. Because of that, the root-mean-square

396 deviation between the Raman-determined and standard $\text{Fe}^{3+}/\text{Fe}^{\text{TOT}}$ values is ± 0.04 when
397 assuming $F_{\text{OX}} = C_{\text{OX}}$. Slightly better results were obtained using eq. 5, which allows
398 $\text{Fe}^{3+}/\text{Fe}^{\text{TOT}}$ of the glasses to be determined within ± 0.03 (Table 1).

399

400 3.2.4 *Neural Networks, Kernel Ridge and Support Vector regression methods*

401

402 The *Neural Network*, *Kernel Ridge*, and *Support Vector* methods performed very well on
403 both the training and testing datasets (Fig. 7), with root-mean-square deviations between the
404 measured and predicted $\text{Fe}^{3+}/\text{Fe}^{\text{TOT}}$ values of ~ 0.01 - 0.03 (Table 1). For all methods, the root-
405 mean-square deviations for the training dataset were slightly lower than that for the testing
406 dataset, indicating that machine-learning algorithms tend to slightly over-fit the training
407 dataset. Over-fitting is not desirable because it indicates that the *generalisation* ability of the
408 algorithms (i.e. their ability to predict values for new samples) may not be optimal. However,
409 in the present case, the difference between the training and testing standard deviations is
410 small (≤ 0.02), and the over-fitting is considered to be negligible. Therefore, these algorithms
411 can be used to predict $\text{Fe}^{3+}/\text{Fe}^{\text{TOT}}$ of MORB glasses with an error $\leq \pm 0.03$ (1σ).

412

413 3.2.5 Is there a better method?

414

415 The root-mean-square deviations between the $\text{Fe}^{3+}/\text{Fe}^{\text{TOT}}$ values determined by
416 Mössbauer and Raman spectroscopy are < 0.04 for all six methods. The *Intensity* and *Mixing*
417 methods are as accurate and precise as those using machine learning (*ALS MCR*, *Neural*
418 *Network*, *Kernel Ridge* and *Support Vector*; Table 1).

419

420 The choice of method depends on the aims of the study and the dataset. If a single data
421 reduction method was to be chosen, the simplicity of the *Intensity* and *Mixing* methods makes
422 these appealing. In the case the $\text{Fe}^{3+}/\text{Fe}^{\text{TOT}}$ of the standards are unknown, the *ALS MCR*
423 method may allow $S_{k,m}$ components to be extracted and the $\text{Fe}^{3+}/\text{Fe}^{\text{TOT}}$ to be determined, if
424 the dataset covers a large range of $\text{Fe}^{3+}/\text{Fe}^{\text{TOT}}$ values (Fig. 5). The *Intensity*, *Mixing* and *ALS*
425 *MCR* methods all rely on linear variations between Raman signals and $\text{Fe}^{3+}/\text{Fe}^{\text{TOT}}$ of the
426 glasses. In contrast, the *Neural Network*, *Kernel Ridge*, and *Support Vector* methods do not
427 assume linear variations and do not require the mathematical form of the variations to be
428 known.

429

430 Ultimately, we recommend the use of multiple data reduction methods, as undertaken
431 here, to test the consistency of results. This is desirable because each data reduction protocol
432 may be differently sensitive to how differences in composition affect the Raman spectra (Fig.
433 2B). Therefore, following a Bayesian approach, the average of the results from all the
434 methods should be more robust than any single estimate (e.g. Perrone, 1993). In the present
435 case, such an approach is easy to implement because all the methods presented in this study
436 are simple to setup and cheap in terms of computing resources. For the present dataset,
437 averaging the results of the six models to obtain an estimate of the $\text{Fe}^{3+}/\text{Fe}^{\text{TOT}}$ from the
438 Raman spectra of the glasses resulted in a root-mean-square deviation of 0.02 (1σ).

439

440 3.2.6 Application to natural MORB glasses

441

442 The baseline subtracted and normalised Raman spectra of natural MORB glasses are shown
443 in Figure 8A (see supplementary Jupyter Notebook for full spectra). While their spectra are
444 similar to that of the glass standard with $\text{Fe}^{3+}/\text{Fe}^{\text{TOT}} = 0.106$, non-negligible differences are
445 apparent (8A). I_{930} varies between 0.64 and 0.76, and is correlated with the concentration of
446 MgO and CaO in the glass (Pearson correlation coefficient = 0.76, Fig. 8B). For the glass
447 standards, a difference of ~ 0.2 in I_{930} corresponds to a difference in $\text{Fe}^{3+}/\text{Fe}^{\text{TOT}}$ of ~ 0.2 (Fig.
448 3). For these spectra, the methods described give an average $\text{Fe}^{3+}/\text{Fe}^{\text{TOT}}$ of 0.16 with a large
449 standard deviation of 0.12.

450

451 It is possible to refine this estimate by including a compositional term in the expressions
452 relating Raman features to $\text{Fe}^{3+}/\text{Fe}^{\text{TOT}}$. We focused on the *Intensity method* and expressed
453 I_{930} as:

454

$$455 I_{930} = (K0 + K1 \times \text{Fe}^{3+}/\text{Fe}^{\text{TOT}}) + K2 \times X, \quad (6)$$

456

457 where X is a parameter reflecting the chemistry of the samples, and K0, K1 and K2 constants.
458 X could be chosen as either [MgO+CaO] or the number of non-bridging oxygen per
459 tetrahedral units (NBO/T) in the glass. Increasing [MgO + CaO] favours the formation of
460 non-bridging oxygens and thus depolymerised Q^2 units in basaltic glasses, which give signals
461 near 950 cm^{-1} (e.g. Mysen et al., 1982). This is consistent with the positive trend observed

462 between I_{930} and $[\text{MgO} + \text{CaO}]$ (Fig. 8B). However, while NBO/T parameterises the general
 463 effect of variations in the fractions of network formers (e.g. Si, Al) and network modifiers
 464 (e.g. Na, K, Ca, Mg) on the glass structure, it does not consider the effect of the ionic
 465 properties of network modifiers on the distribution of Q^n units, which contribute to the
 466 Raman intensity between 850 and 1140 cm^{-1} . For example, at a constant NBO/T of 0.5, the
 467 fractions of Q^4 and Q^2 increase at the expense of that of Q^3 in alkali silicate glasses as the
 468 ionic field strength (Z/r^2 , where Z is the electric charge and r the ionic radius) of the alkali
 469 metal cation increases (Maekawa et al., 1991). The ionic field strength of metal cations also
 470 influences many other structural properties of silicate glasses and melts, including the
 471 fraction of highly-coordinated Al, excess NBO, and Si-Al disorder (see Le Losq et al., 2019
 472 for a review). As a result, to capture changes in the Raman spectra due to variations in the
 473 sample chemistry, we used the mean ionic field strength (IFS) of network modifiers (M),
 474 $\text{IFS}(\text{M})$, as the X parameter in eq. (6):

475

$$476 \text{IFS}(\text{M}) = 2x_{\text{Na}_2\text{O}} \times \text{IFS}(\text{Na}^+) + 2x_{\text{K}_2\text{O}} \times \text{IFS}(\text{K}^+) + x_{\text{CaO}} \times \text{IFS}(\text{Ca}^{2+}) + x_{\text{MgO}} \times$$

$$477 \text{IFS}(\text{Mg}^{2+}) + x_{\text{FeO}} \times \text{IFS}(\text{Fe}^{2+}), \quad (7)$$

478

479 where $x_{M_{2/z}^{z+}O}$ are the mol fractions of the oxide components $M_{2/z}^{z+}O$, and IFS is the ionic field
 480 strength of the cation M^{z+} , calculated as Z/r^2 . The r values were taken from Shannon (1976),
 481 with coordination numbers (CN) of 6 for all M cations. For simplicity, we do not consider
 482 variations in CN although they will vary with glass composition (Le Losq et al., 2019 and
 483 references therein), but probably this effect is negligible due to limited range of
 484 compositional variability of MORB. We also consider FeO as equal to total Fe because the
 485 $\text{Fe}^{3+}/\text{Fe}^{\text{TOT}}$ ratio of natural MORB is always low (~ 0.1) and constant (e.g. Berry et al., 2018;
 486 Zhang et al., 2018), such that any influence of Fe on the glass structure will come from
 487 variations in x_{FeO} .

488

489 The correlation between I_{930} and $\text{IFS}(\text{M})$ is linear for natural MORB glasses (Fig. 9). The
 490 ordinate at the origin of this trend corresponds to $\text{K0} + \text{K1} \times \text{Fe}^{3+}/\text{Fe}^{\text{TOT}}$, and its slope to K2.
 491 K1 is directly given by the linear trend between $\text{Fe}^{3+}/\text{Fe}^{\text{TOT}}$ and I_{930} (Fig. 3), and is equal to
 492 0.2435(23), while K2 equals 0.00624(29). It then is trivial to determine K0 as 0.111(27).
 493 Using these parameters, it is possible to plot iso-redox curves of $\text{IFS}(\text{M})$ versus I_{930} , as shown
 494 in Fig. 9. A visual inspection indicates that the natural samples have a mean $\text{Fe}^{3+}/\text{Fe}^{\text{TOT}}$ value

495 ~ 0.1, although there is significant scatter. Manipulating eq. (7) to extract $\text{Fe}^{3+}/\text{Fe}^{\text{TOT}}$ values
496 for natural MORB from K0, K1, K2 and I₉₃₀ yields a mean $\text{Fe}^{3+}/\text{Fe}^{\text{TOT}}$ of 0.090(67).

497

498 **4. Discussion**

499

500 Both conventional methods (*Intensity, Mixing*) and machine learning algorithms (*ALS MCR,*
501 *Kernel Ridge, Support Vector* and *Neural Network*) allow $\text{Fe}^{3+}/\text{Fe}^{\text{TOT}}$ to be determined from
502 the Raman spectra of glasses, with fixed major element composition, with uncertainties <
503 0.04 (Table 1). The combination of all six methods gives a precision of 0.02. The *Intensity*
504 and *Mixing* methods are simple and provide accurate results. The machine learning methods
505 performed well despite being trained with a limited set of samples. The *ALS MCR* method
506 may be useful if the $\text{Fe}^{3+}/\text{Fe}^{\text{TOT}}$ values of the glass standards are unknown, or if endmember
507 spectra are not available. *Kernel Ridge, Support Vector* and *Neural Network* regression
508 algorithms relate $\text{Fe}^{3+}/\text{Fe}^{\text{TOT}}$ of the glasses to variations in their Raman spectra without any
509 assumptions about the form of the variations. Pooling the results from multiple data reduction
510 protocols is recommended for maximizing the robustness of $\text{Fe}^{3+}/\text{Fe}^{\text{TOT}}$ determinations for
511 glasses with fixed composition.

512

513 The determination of $\text{Fe}^{3+}/\text{Fe}^{\text{TOT}}$ in natural MORB glasses requires a correction for the effect
514 of composition on the Raman spectra (Figs. 8B, 9, eq. 7). The corrected mean value of
515 $\text{Fe}^{3+}/\text{Fe}^{\text{TOT}} = 0.090(67)$ is in agreement with the latest XANES and wet chemistry
516 measurements (Bézos and Humler, 2005; Berry et al., 2018; Zhang et al., 2018). In particular,
517 this estimate is in close agreement with the XANES estimate of 0.10(1) reported by Berry et
518 al. (2018) for the same set of samples, which suggests an average fO_2 for MORB of 0.1 above
519 the quart-fayalite-magnetite redox buffer.

520

521 Raman spectroscopy can thus provide reasonable estimates of $\text{Fe}^{3+}/\text{Fe}^{\text{TOT}}$ in glasses, as long
522 as the effect of glass chemistry is considered. However, the present results do not achieve the
523 precision of Fe K-edge XANES, Mössbauer spectroscopy or wet chemistry for natural
524 samples with variable chemical composition. While eq. (6) is valid for MORB glasses, it is
525 probably not suitable for determining $\text{Fe}^{3+}/\text{Fe}^{\text{TOT}}$ in other compositions. However, with a set
526 of appropriate standards, Raman spectroscopy could be used to quantify $\text{Fe}^{3+}/\text{Fe}^{\text{TOT}}$ in any
527 composition through the use of a chemical correction similar to that of eq. (6).

528

529 **5. Implications**

530

531 Machine learning techniques do not seem to be advantageous relative to conventional
532 approaches for quantifying $\text{Fe}^{3+}/\text{Fe}^{\text{TOT}}$ in glasses with fixed standard composition by Raman
533 spectroscopy. However, their ease of implementation and flexibility (the problem can be
534 linear or not) make them preferable to other user-defined techniques when the functional
535 form of the problem is unknown. In particular, the sensitivity of Raman spectra to glass
536 structure can be used to determine glass composition. Di Genova et al. (2015; 2016) proposed
537 use of the mixing method to determine the composition of natural glasses from their Raman
538 spectra. This required a post-analysis step in the data treatment as the mixing ratio of end-
539 member spectra varied non-linearly with glass composition. In the present case, we trained a
540 neural network to directly link the corrected 850-1140 cm^{-1} Raman signals (Fig. 8A) to the
541 measured concentrations of major elements in the natural MORB glasses (supplementary
542 materials), without any additional data manipulation. The results from one of the trained
543 neural networks are shown in Figure 10. The network was able to predict the chemistry of
544 MORB glasses with maximum errors of ~ 1 mol%. This result suggests that Raman
545 spectroscopy may be developed as a chemical probe. It also demonstrates the usefulness of
546 neural networks for such calculations, as the algorithm directly provides the glass
547 composition without intermediate data analysis steps, as required by the method of Di
548 Genova et al. (2015; 2016). The approach could allow Raman spectroscopy to be used *in situ*
549 to analyse erupting basalts forming pillow lavas with glassy rims at ocean ridges, using
550 submersibles equipped with Raman spectrometers already developed for deep sea water
551 analysis (e.g. Brewer et al., 2004; White et al., 2005; Du et al., 2015), or for using Raman
552 spectrometers as chemical probes during missions on planets or moons with dense
553 atmospheres. The fact that all data processing performed in this study uses Python, a
554 programming language that can be easily used in embedded systems would facilitate uptake.
555 The present approach should be easy to implement in any system operating a portable Raman
556 spectrometer.

557

558 **Acknowledgement**

559

560 The Department of Mineral Sciences, Smithsonian Institution, is thanked for providing the
561 samples of MORB glass. H.O.N thanks the Australian Research Council for the award of a
562 Laureate Fellowship (FL130100066). C.L.L. thanks Guil Malmann for helpful discussions.

564 **References**

565

- 566 Asimow, P.D., Dixon, J.E., Langmuir, C.H., 2004. A hydrous melting and fractionation
567 model for mid-ocean ridge basalts: Application to the Mid-Atlantic Ridge near the
568 Azores. *Geochem. Geophys. Geosystems* 5. <https://doi.org/10.1029/2003GC000568>
- 569 Behrens, H., Roux, J., Neuville, D., Siemann, M., 2006. Quantification of dissolved H₂ O in
570 silicate glasses using confocal microRaman spectroscopy. *Chem. Geol.* 229, 96–112.
- 571 Bengio, Y., 2009. Learning Deep Architectures for AI. *Found. Trends® Mach. Learn.* 2, 1–
572 127. <https://doi.org/10.1561/22000000006>
- 573 Berry, A.J., Danyushevsky, L.V., O'Neill, H.S.C., Newville, M., Sutton, S.R., 2008.
574 Oxidation state of iron in komatiitic melt inclusions indicates hot Archaean mantle.
575 *Nature* 455, 960–963. <https://doi.org/10.1038/nature07377>
- 576 Berry, A.J., Stewart, G.A., O'Neill, H.S.C., Mallmann, G., Mosselmans, J.F.W., 2018. A re-
577 assessment of the oxidation state of iron in MORB glasses. *Earth Planet. Sci. Lett.*
578 483, 114–123. <https://doi.org/10.1016/j.epsl.2017.11.032>
- 579 Bézou, A., Humler, E., 2005. The Fe³⁺/ΣFe ratios of MORB glasses and their implications for
580 mantle melting. *Geochim. Cosmochim. Acta* 69, 711–725.
581 <https://doi.org/10.1016/j.gca.2004.07.026>
- 582 Brawer, S.A., White, W.B., 1977. Raman spectroscopic investigation of the structure of
583 silicate glasses (II). Soda-alkaline earth-alumina ternary and quaternary glasses. *J.*
584 *Non-Cryst. Solids* 23, 261–278. [https://doi.org/10.1016/0022-3093\(77\)90009-6](https://doi.org/10.1016/0022-3093(77)90009-6)
- 585 Brawer, S.A., White, W.B., 1975. Raman spectroscopic investigation of the structure of
586 silicate glasses. I. The binary alkali silicates. *J. Chem. Phys.* 63, 2421–2432.
587 <https://doi.org/10.1063/1.431671>
- 588 Breiman, L., Breiman, L., 1996. Bagging Predictors, in: *Machine Learning*. pp. 123–140.
- 589 Brewer, P.G., Malby, G., Pasteris, J.D., White, S.N., Peltzer, E.T., Wopenka, B., Freeman, J.,
590 Brown, M.O., 2004. Development of a laser Raman spectrometer for deep-ocean
591 science. *Deep Sea Res. Part Oceanogr. Res. Pap.* 51, 739–753.
592 <https://doi.org/10.1016/j.dsr.2003.11.005>
- 593 Christie, D.M., Carmichael, I.S.E., Langmuir, C.H., 1986. Oxidation states of mid-ocean
594 ridge basalt glasses. *Earth Planet. Sci. Lett.* 79, 397–411.
595 [https://doi.org/10.1016/0012-821X\(86\)90195-0](https://doi.org/10.1016/0012-821X(86)90195-0)
- 596 Cochain, B., Neuville, D.R., Henderson, G.S., McCammon, C.A., Pinet, O., Richet, P., 2012.
597 Effects of the iron content and redox state on the structure of sodium borosilicate
598 glasses: A Raman, Mössbauer and boron K-Edge XANES spectroscopy study. *J. Am.*
599 *Ceram. Soc.* 95, 962–971.
- 600 Cottrell, E., Kelley, K.A., 2013. Redox heterogeneity in mid-ocean ridge basalts as a function
601 of mantle source. *Science* 340, 1314–1317. <https://doi.org/10.1126/science.1233299>
- 602 Cottrell, E., Kelley, K.A., 2011. The oxidation state of Fe in MORB glasses and the oxygen
603 fugacity of the upper mantle. *Earth Planet. Sci. Lett.* 305, 270–282.
604 <https://doi.org/10.1016/j.epsl.2011.03.014>
- 605 Cottrell, E., Lanzirrotti, A., Mysen, B.O., Birner, S., Kelley, K.A., Botcharnikov, R.E., Davis,
606 F.A., Newville, M., in press. A Mössbauer-based XANES calibration for hydrous
607 basalt glasses reveals radiation-induced oxidation of Fe. *Am. Mineral.*
608 <https://doi.org/10.2138/am-2018-6268>
- 609 de Juan, A., Tauler, R., 2006. Multivariate Curve Resolution (MCR) from 2000: Progress in
610 Concepts and Applications. *Crit. Rev. Anal. Chem.* 36, 163–176.
611 <https://doi.org/10.1080/10408340600970005>

612 Di Genova, D., Hess, K.-U., Chevrel, M.O., Dingwell, D.B., 2016. Models for the estimation
613 of $\text{Fe}^{3+}/\text{Fe}^{\text{tot}}$ ratio in terrestrial and extraterrestrial alkali- and iron-rich silicate glasses
614 using Raman spectroscopy. *Am. Mineral.* 101, 943–952.

615 Di Genova, Danilo, Kolzenburg, S., Vona, A., Chevrel, M.O., Hess, K.-U., Neuville, D.R.,
616 Ertel-Ingrisch, W., Romano, C., Dingwell, D.B., 2016. Raman spectra of Martian
617 glass analogues: A tool to approximate their chemical composition. *J. Geophys. Res.*
618 *Planets* 121, 2016JE005010. <https://doi.org/10.1002/2016JE005010>

619 Di Genova, D., Morgavi, D., Hess, K.-U., Neuville, D.R., Borovkov, N., Perugini, D.,
620 Dingwell, D.B., 2015. Approximate chemical analysis of volcanic glasses using
621 Raman spectroscopy. *J. Raman Spectrosc.* 46, 1235–1244.
622 <https://doi.org/10.1002/jrs.4751>

623 Di Genova, D., Sicola, S., Romano, C., Vona, A., Fanara, S., Spina, L., 2017. Effect of iron
624 and nanolites on Raman spectra of volcanic glasses: A reassessment of existing
625 strategies to estimate the water content. *Chem. Geol.* 475, 76–86.
626 <https://doi.org/10.1016/j.chemgeo.2017.10.035>

627 Di Muro, A., Métrich, N., Mercier, M., Giordano, D., Massare, D., Montagnac, G., 2009.
628 Micro-Raman determination of iron redox state in dry natural glasses: Application to
629 peralkaline rhyolites and basalts. *Chem. Geol.* 259, 78–88.
630 <https://doi.org/10.1016/j.chemgeo.2008.08.013>

631 Du, Z., Li, Y., Chen, J., Guo, J., Zheng, R., 2015. Feasibility investigation on deep ocean
632 compact autonomous Raman spectrometer developed for in-situ detection of acid
633 radical ions. *Chin. J. Oceanol. Limnol.* 33, 545–550. [https://doi.org/10.1007/s00343-](https://doi.org/10.1007/s00343-015-4096-8)
634 [015-4096-8](https://doi.org/10.1007/s00343-015-4096-8)

635 Eilers, P.H.C., 2003. A perfect smoother. *Anal. Chem.* 75, 3631–3636.
636 <https://doi.org/10.1021/ac034173t>

637 Furukawa, T., Fox, K.E., White, W.B., 1981. Raman spectroscopic investigation of the
638 structure of silicate glasses. III. Raman intensities and structural units in sodium
639 silicate glasses. *J. Chem. Phys.* 75, 3226–3237. <https://doi.org/10.1063/1.442472>

640 Furukawa, T., White, W.B., 1980. Vibrational spectra and glass structure. *J. Non-Cryst.*
641 *Solids* 38, 87–92.

642 Gale, A., Dalton, C.A., Langmuir, C.H., Su, Y., Schilling, J.-G., 2013. The mean composition
643 of ocean ridge basalts. *Geochem. Geophys. Geosystems* 14, 489–518.
644 <https://doi.org/10.1029/2012GC004334>

645 Galeener, F.L., Sen, P.N., 1978. Theory of the first-order vibrational spectra of disordered
646 solids. *Phys. Rev. B* 17, 1928–1933.

647 Glorot, X., Bordes, A., Bengio, Y., 2011. Deep sparse rectifier neural networks, in:
648 *International Conference on Artificial Intelligence and Statistics*. pp. 315–323.

649 Hyvärinen, A., Karhunen, J., Oja, E., 2001. *Independent component analysis*. John Wiley &
650 *Sons, Inc.*

651 Jenner, F.E., O'Neill, H.S.C., 2012. Analysis of 60 elements in 616 ocean floor basaltic
652 glasses: TECHNICAL BRIEF. *Geochem. Geophys. Geosystems* 13, n/a-n/a.
653 <https://doi.org/10.1029/2011GC004009>

654 Jiang, J.-H., Liang, Y., Ozaki, Y., 2004. Principles and methodologies in self-modeling curve
655 resolution. *Chemom. Intell. Lab. Syst.* 71, 1–12.
656 <https://doi.org/10.1016/j.chemolab.2003.07.002>

657 Kendrick, M.A., Arculus, R., Burnard, P., Honda, M., 2013. Quantifying brine assimilation
658 by submarine magmas: Examples from the Galápagos Spreading Centre and Lau
659 Basin. *Geochim. Cosmochim. Acta* 123, 150–165.
660 <https://doi.org/10.1016/j.gca.2013.09.012>

661 Langmuir, C.H., Klein, E.M., Plank, T., 1992. Petrological Systematics of Mid-Ocean Ridge
662 Basalts: Constraints on Melt Generation Beneath Ocean Ridges, in: Mantle Flow and
663 Melt Generation at Mid-Ocean Ridges, Geophysical Monograph. American
664 Geophysical Union (AGU), pp. 183–280. <https://doi.org/10.1029/GM071p0183>

665 Le Losq, C., 2018. Rumpy: a Python library for processing spectroscopic (IR, Raman,
666 XAS...) data. Zenodo. <https://doi.org/10.5281/zenodo.1168730>

667 Le Losq, C., Cicconi, M.R., Greaves, G.N., Neuville, D.R., 2019. Silicate Glasses, in:
668 Handbook of Glass. Springer.

669 Le Losq, C., Neuville, D.R., 2013. Effect of the Na/K mixing on the structure and the
670 rheology of tectosilicate silica-rich melts. *Chem. Geol.* 346, 57–71.
671 <http://dx.doi.org/10.1016/j.chemgeo.2012.09.009>

672 Le Losq, C., Neuville, D.R., Florian, P., Henderson, G.S., Massiot, D., 2014. The role of Al³⁺
673 on rheology and structural changes of sodium silicate and aluminosilicate glasses and
674 melts. *Geochim. Cosmochim. Acta* 126, 495–517.
675 <https://doi.org/10.1016/j.gca.2013.11.010>

676 Le Losq, C., Neuville, D.R., Moretti, R., Roux, J., 2012. Determination of water content in
677 silicate glasses using Raman spectrometry: Implications for the study of explosive
678 volcanism. *Am. Mineral.* 97, 779–790. <https://doi.org/10.2138/am.2012.3831>

679 Lin, C.-J., 2007. Projected Gradient Methods for Nonnegative Matrix Factorization. *Neural*
680 *Comput.* 19, 2756–2779. <https://doi.org/10.1162/neco.2007.19.10.2756>

681 Maekawa, H., Maekawa, T., Kawamura, K., Yokokawa, T., 1991. The structural groups of
682 alkali silicate glasses determined from ²⁹Si MAS-NMR. *J. Non-Cryst. Solids* 127, 53–
683 64. [https://doi.org/10.1016/0022-3093\(91\)90400-Z](https://doi.org/10.1016/0022-3093(91)90400-Z)

684 Magnien, V., Neuville, D., Cormier, L., Roux, J., Hazemann, J., Deligny, D., Pascarelli, S.,
685 Vickridge, I., Pinet, O., Richet, P., 2008. Kinetics and mechanisms of iron redox
686 reactions in silicate melts: The effects of temperature and alkali cations. *Geochim.*
687 *Cosmochim. Acta* 72, 2157–2168.

688 Magnien, V., Neuville, D.R., Cormier, L., Mysen, B.O., Briois, V., Belin, S., Pinet, O.,
689 Richet, P., 2004. Kinetics of iron oxidation in silicate melts: a preliminary XANES
690 study. *Chem. Geol.* 213, 253–263.

691 Magnien, V., Neuville, D.R., Cormier, L., Roux, J., Hazemann, J.L., Pinet, O., Richet, P.,
692 2006. Kinetics of iron redox reactions in silicate liquids: A high-temperature X-ray
693 absorption and Raman spectroscopy study. *J. Nucl. Mater.* 352, 190–195.

694 McMillan, P.F., 1984. Structural studies of silicate glasses and melts - Applications and
695 limitations of Raman spectroscopy. *Am. Mineral.* 69, 622–644.

696 Melson, W.G., O’Hearn, T., Jarosewich, E., 2002. A data brief on the Smithsonian Abyssal
697 Volcanic Glass Data File. *Geochem. Geophys. Geosystems* 3, 1–11.
698 <https://doi.org/10.1029/2001GC000249>

699 Mercier, M., Di Muro, A., Giordano, D., Métrich, N., Lesne, P., Pichavant, M., Scaillet, B.,
700 Clocchiatti, R., Montagnac, G., 2009. Influence of glass polymerisation and oxidation
701 on micro-Raman water analysis in alumino-silicate glasses. *Geochim. Cosmochim.*
702 *Acta* 73, 197–217. <https://doi.org/10.1016/j.gca.2008.09.030>

703 Mercier, M., Muro, A.D., Métrich, N., Giordano, D., Belhadj, O., Mandeville, C.W., 2010.
704 Spectroscopic analysis (FTIR, Raman) of water in mafic and intermediate glasses and
705 glass inclusions. *Geochim. Cosmochim. Acta* 74, 5641–5656.
706 <https://doi.org/10.1016/j.gca.2010.06.020>

707 Métrich, N., Bertagnini, A., Garaebiti, E., Vergnolle, S., Bani, P., Beaumais, A., Neuville,
708 D.R., 2016. Magma transfer and degassing budget: Application to the 2009–2010
709 eruptive crisis of Mt Garet (Vanuatu arc). *J. Volcanol. Geotherm. Res.* 322, 48–62.
710 <https://doi.org/10.1016/j.jvolgeores.2015.06.003>

711 Morizet, Y., Brooker, R.A., Iacono-Marziano, G., Kjarsgaard, B.A., 2013. Quantification of
712 dissolved CO₂ in silicate glasses using micro-Raman spectroscopy. *Am. Mineral.* 98,
713 1788–1802. <https://doi.org/10.2138/am.2013.4516>

714 Murphy, K.P., 2012. *Machine Learning: A Probabilistic Perspective*. The MIT Press,
715 Cambridge, Massachusetts.

716 Mysen, B.O., 1990. Role of Al in depolymerized, peralkaline aluminosilicate melts in the
717 systems Li₂ O-Al₂ O₃ -SiO₂ , Na₂ O-Al₂ O₃ -SiO₂ , and K₂ O-Al₂ O₃ -SiO₂ . *Am.*
718 *Mineral.* 75, 120–134.

719 Mysen, B.O., Finger, L.W., Virgo, D., Seifert, F.A., 1982. Curve-fitting of Raman spectra of
720 silicate glasses. *Am. Mineral.* 67, 686–695.

721 Mysen, B.O., Lucier, A., Cody, G.D., 2003. The structural behavior of Al³⁺ in peralkaline
722 melts and glasses in the system Na₂ O-Al₂ O₃ -SiO₂ . *Am. Mineral.* 88, 1668–1678.

723 Mysen, B.O., Richet, P., 2005. *Silicate glasses and melts - Properties and structure,*
724 *Developments in geochemistry*. Elsevier B.V., Amsterdam.

725 Neuville, D.R., Mysen, B.O., 1996. Role of aluminium in the silicate network: In situ, high-
726 temperature study of glasses and melts on the join SiO₂-NaAlO₂. *Geochim.*
727 *Cosmochim. Acta* 60, 1727–1737.

728 O'Neill, H.S.C., Berry, A.J., Mallmann, G., 2018. The oxidation state of iron in Mid-Ocean
729 Ridge basaltic (MORB) glasses: implications for their petrogenesis and oxygen
730 fugacities. *Earth Planet. Sci. Lett.* 504, 152–162.

731 O'Neill, H.S.C., Jenner, F.E., 2012. The global pattern of trace-element distributions in ocean
732 floor basalts. *Nature* 491, 698–704. <https://doi.org/10.1038/nature11678>

733 Pedregosa, F., Varoquaux, G., Gramfort, A., Michel, V., Thirion, B., Grisel, O., Blondel, M.,
734 Prettenhofer, P., Weiss, R., Dubourg, V., Vanderplas, J., Passos, A., Cournapeau, D.,
735 Brucker, M., Perrot, M., Duchesnay, E., 2011. Scikit-learn: machine learning in
736 python. *J. Mach. Learn. Res.* 12, 2825–2830.

737 Perrone, M.P., 1993. *Improving regression estimation: Averaging methods for variance*
738 *reduction with extensions to general convex measure optimization*. Brown University
739 Providence, RI.

740 Roskosz, M., Toplis, M.J., Neuville, D.R., Mysen, B.O., 2008. Amorphous materials:
741 Properties, structure, and durability: Quantification of the kinetics of iron oxidation in
742 silicate melts using Raman spectroscopy and assessment of the role of oxygen
743 diffusion. *Am. Mineral.* 93, 1749–1759. <https://doi.org/10.2138/am.2008.2861>

744 Shannon, R.D., 1976. Revised effective ionic radii and systematic studies of interatomic
745 distances in halides and chalcogenides. *Acta Crystallogr. A* 32, 751–767.
746 <https://doi.org/10.1107/S0567739476001551>

747 Shea, T., Hellebrand, E., Gurioli, L., Tuffen, H., 2014. Conduit- to Localized-scale Degassing
748 during Plinian Eruptions: Insights from Major Element and Volatile (Cl and H₂O)
749 Analyses within Vesuvius AD 79 Pumice. *J. Petrol.* 55, 315–344.
750 <https://doi.org/10.1093/petrology/egt069>

751 Smola, A. J., Schölkopf, B., 2004. A tutorial on support vector regression. *Stat. Comput.* 14,
752 199–222.

753 Tarantola, A., 2005. *Inverse problem theory and methods for model parameter estimation*.
754 Society for Industrial and Applied Mathematics, Philadelphia, PA.

755 Thomas, R., 2000. Determination of water contents of granite melt inclusions by confocal
756 laser Raman microprobe spectroscopy. *Am. Mineral.* 85, 868–872.

757 Thomas, R., Metrich, N., Scaillet, B., Kamenetsky, V.S., Davidson, P., 2008. Determination
758 of water in Fe-rich basalt glasses with confocal micro-Raman spectroscopy. *Z. Für*
759 *Geol. Wiss.* 36, 31–37.

760 Valderrama, L., Gonçalves, R.P., Março, P.H., Rutledge, D.N., Valderrama, P., 2016.
761 Independent components analysis as a means to have initial estimates for multivariate
762 curve resolution-alternating least squares. *J. Adv. Res.* 7, 795–802.
763 <https://doi.org/10.1016/j.jare.2015.12.001>

764 Vapnik, V. N., 1999. *The Nature of Statistical Learning Theory, Second Edition.* ed.
765 Springer-Verlag, New York.

766 Virgo, D., Mysen, B. O., Danckwerth, P., Seifert, F., 1982. Speciation of Fe³⁺ in 1-atm Na₂O-
767 SiO₂-Fe-O Melts. *Carnegie Inst. Wash. Year b.* 81, 349–353.

768 Virgo, D., Mysen, B.O., Kushiro, I., 1980. Anionic constitution of 1-Atmosphere silicate
769 melts: implications for the structure of igneous melts. *Science* 208, 1371–1373.
770 <https://doi.org/10.1126/science.208.4450.1371>

771 Wang, Z., Cooney, T.F., Sharma, S.K., 1995. In situ structural investigation of iron-
772 containing silicate liquids and glasses. *Geochim. Cosmochim. Acta* 59, 1571–1577.
773 [https://doi.org/10.1016/0016-7037\(95\)00063-6](https://doi.org/10.1016/0016-7037(95)00063-6)

774 Welsch, A.-M., Knipping, J.L., Behrens, H., 2017. Fe-oxidation state in alkali-trisilicate
775 glasses - A Raman spectroscopic study. *J. Non-Cryst. Solids* 471, 28–38.
776 <https://doi.org/10.1016/j.jnoncrysol.2017.04.033>

777 White, S.N., Kirkwood, W., Sherman, A., Brown, M., Henthorn, R., Salamy, K., Walz, P.,
778 Peltzer, E.T., Brewer, P.G., 2005. Development and deployment of a precision
779 underwater positioning system for in situ laser Raman spectroscopy in the deep ocean.
780 *Deep Sea Res. Part Oceanogr. Res. Pap.* 52, 2376–2389.
781 <https://doi.org/10.1016/j.dsr.2005.09.002>

782 Zajacz, Z., Halter, W., Malfait, W.J., Bachmann, O., Bodnar, R.J., Hirschmann, M.M.,
783 Mandeville, C.W., Morizet, Y., Müntener, O., Ulmer, P., Webster, J.D., 2005. A
784 composition-independent quantitative determination of the water content in silicate
785 glasses and silicate melt inclusions by confocal Raman spectroscopy. *Contrib.*
786 *Mineral. Petrol.* 150, 631–642. <https://doi.org/10.1007/s00410-005-0040-9>

787 Zakaznova-Herzog, V.P., Malfait, W.J., Herzog, F., Halter, W.E., 2007. Quantitative Raman
788 spectroscopy: Principles and application to potassium silicate glasses. *J. Non-Cryst.*
789 *Solids* 353, 4015–4028. <https://doi.org/10.1016/j.jnoncrysol.2007.06.033>

790 Zhang, H.L., Cottrell, E., Solheid, P.A., Kelley, K.A., Hirschmann, M.M., 2018.
791 Determination of Fe³⁺/ΣFe of XANES basaltic glass standards by Mössbauer
792 spectroscopy and its application to the oxidation state of iron in MORB. *Chem. Geol.*
793 479, 166–175. <https://doi.org/10.1016/j.chemgeo.2018.01.006>

794
795

796 **Table 1:** Synthesis oxygen fugacity at 1400 °C, and relative to the quartz-fayalite-magnetite
797 (QFM) buffer, of MORB glass standards (Berry et al., 2018), together with the $\text{Fe}^{3+}/\text{Fe}^{\text{TOT}}$
798 values determined by Mössbauer spectroscopy (± 0.01), and by Raman spectroscopy using
799 the Intensity (Int.), Mixing (Mix.), ALS MCR (A.M.), Neural Networks (N.N.), Kernel Ridge
800 (K.R.) and Support Vector (S.V.) techniques. Root-mean-squared deviations (RMSD, 1σ) of
801 the different Raman methods are indicated at the bottom; *calculated for the training data
802 subset; ϕ calculated for the testing data subset.

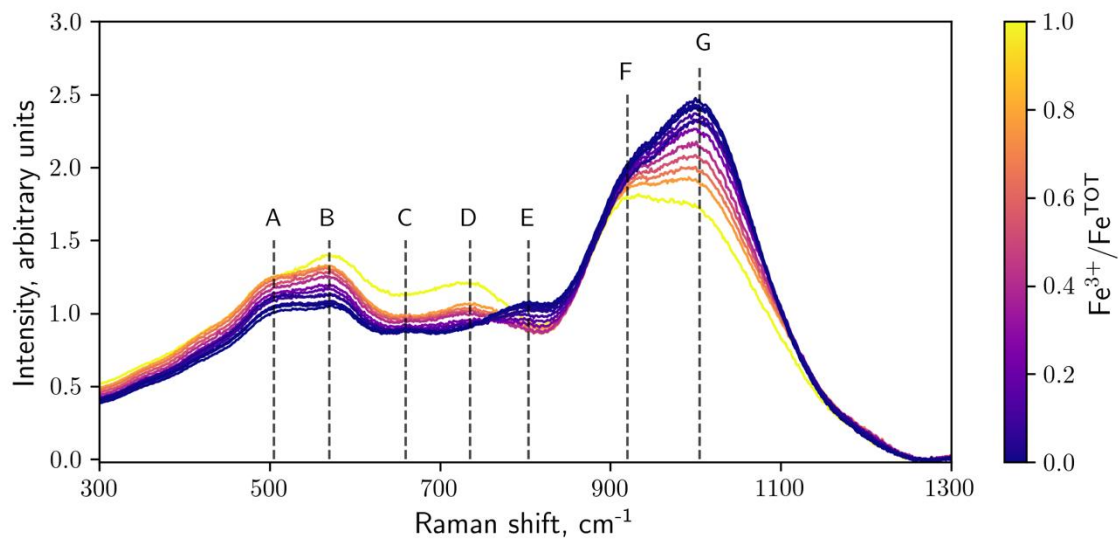
803

log fO ₂	ΔQFM	$\text{Fe}^{3+}/\text{Fe}^{\text{TOT}}$						
		Mössbauer	Int.	Mix.	A.M.	N.N.	K.R.	S.V.
4.8	11.2	1.000	1.01	0.99	1.01	0.97	1.00	0.97
0.00	6.38	0.773	0.75	0.73	0.75	0.77	0.77	0.75
-1.00	5.40	0.661	0.66	0.63	0.65	0.66	0.66	0.66
-2.00	4.40	0.537	0.53	0.51	0.53	0.54	0.54	0.54
-3.07	3.32	0.414	0.43	0.42	0.43	0.43	0.42	0.44
-4.00	2.39	0.250	0.26	0.25	0.27	0.23	0.27	0.28
-5.00	1.39	0.167	0.16	0.15	0.16	0.14	0.16	0.17
-6.00	0.39	0.103	0.11	0.10	0.11	0.09	0.10	0.10
-7.00	-0.61	0.039	0.01	0.01	0.01	0.05	0.04	0.05
-8.00	-1.61	0.024	0.04	0.04	0.05	0.04	0.03	0.02
-9.00	-2.61	0.017	0.02	0.00	0.01	0.03	0.02	0.01
-10.00	-3.61	0.000	0.00	0.00	-0.01	0.02	0.01	-0.01
-11.00	-4.61	0.000	0.01	0.03	0.01	0.01	0.00	0.01
		RMSD:	0.02	0.03	0.03	0.01*	0.01*	0.02*
						0.04 ϕ	0.02 ϕ	0.03 ϕ

804

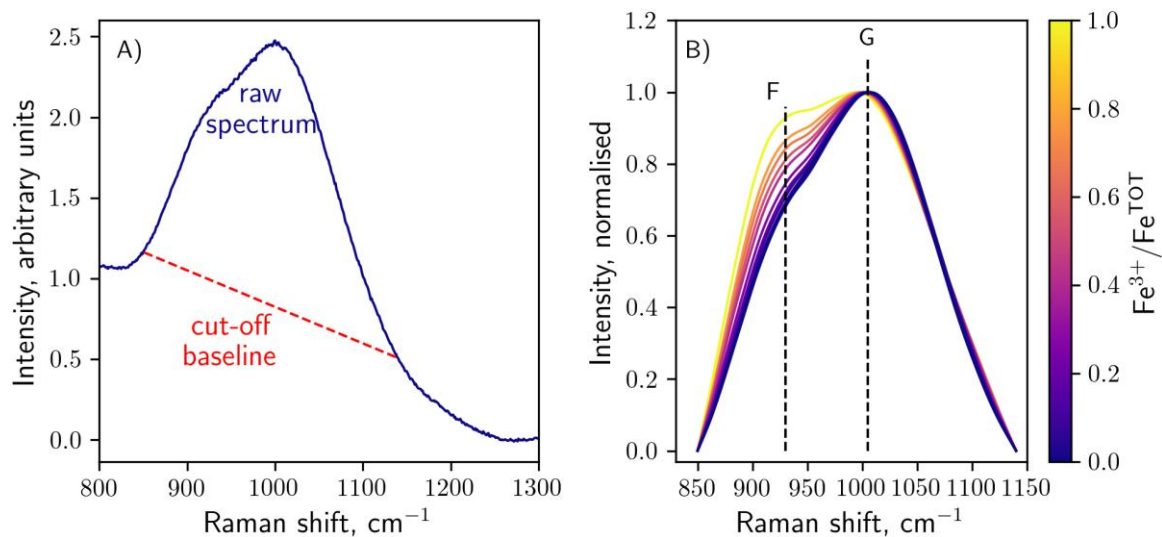
805

806 **Figure 1:** Raman spectra of synthetic MORB basaltic glasses; the colors indicate $\text{Fe}^{3+}/\text{Fe}^{\text{TOT}}$.
807 Each spectrum corresponds to the mean of five spectra acquired for each sample. The dashed
808 lines labelled A-G mark the position of peaks and shoulders (see text).
809



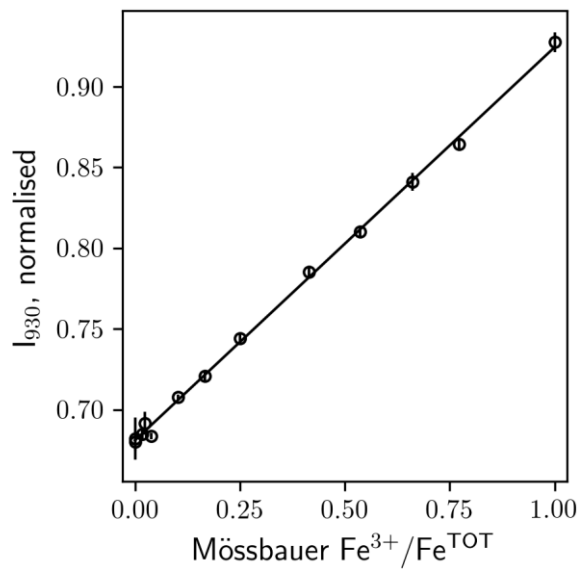
810
811
812

813 **Figure 2:** A) Example of the treatment of the 800-1300 cm^{-1} sections of the Raman spectra
814 that was performed prior to any calculation. The linear cut-off baseline (red dotted line) joins
815 the sample signals at 850 and 1140 cm^{-1} . Any intensity below this baseline is removed from
816 the data. B) Intensity from 850-1140 cm^{-1} after baseline subtraction. This background
817 subtracted region of the spectra was normalised between 0 and 1.
818



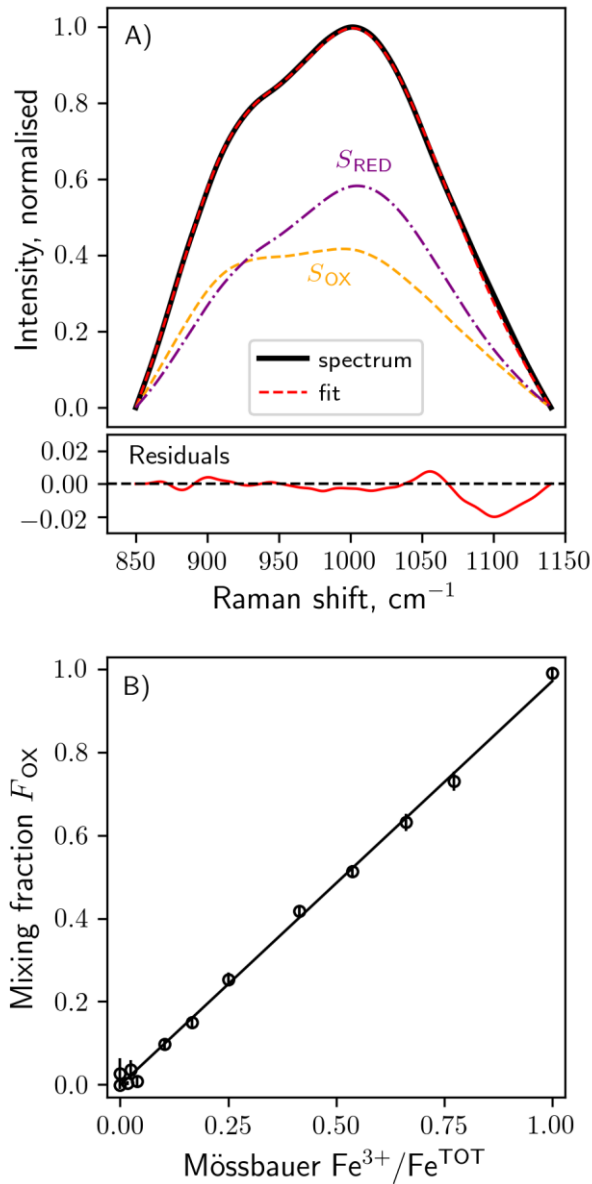
819
820
821

822 **Figure 3:** Normalised intensity at 930 cm^{-1} in the Raman spectra of the glasses as a function
823 of the oxidation state of Fe. The line is a linear fit to the data. If not visible, errors are smaller
824 than the symbols.



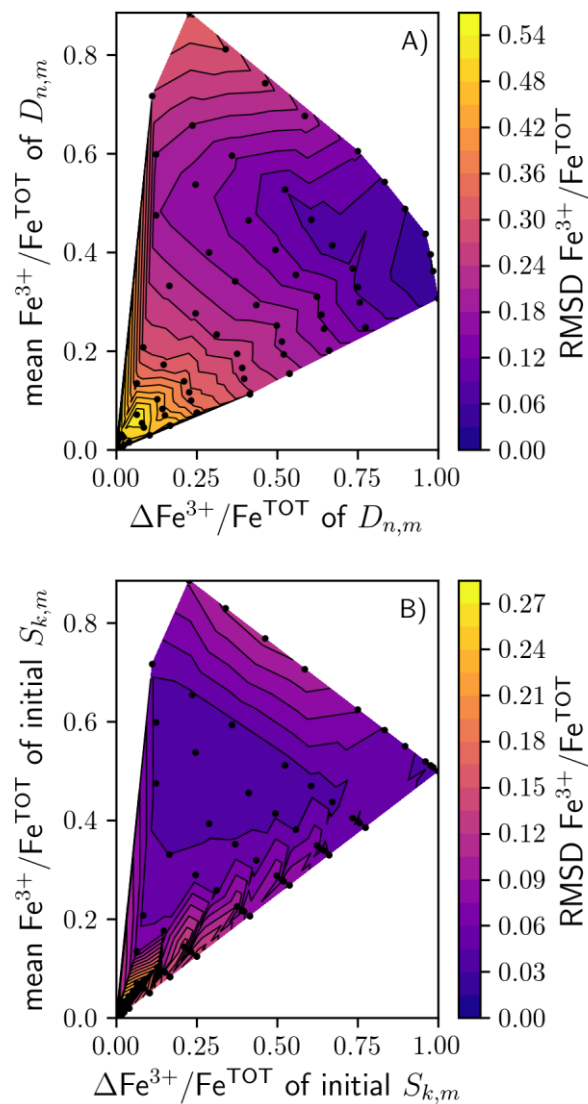
825
826
827
828

829 **Figure 4:** A) Comparison of the mean spectrum at $\text{Fe}^{3+}/\text{Fe}^{\text{TOT}} = 0.41$ (black line) and of fit
 830 (dotted red line) as a linear combination of the oxidised (S_{OX}) and reduced (S_{RED}) spectra
 831 (*Mixing* method); residuals between the data and fit are shown in the bottom panel. B)
 832 Fraction of the oxidised endmember spectrum, F_{OX} , as a function of the oxidation state of Fe
 833 in the glasses. The line is a linear fit to the data. If not visible, errors are smaller than the
 834 symbols.
 835



836
 837
 838
 839

840 **Figure 5:** Results of the tests performed with the *ALS MCR* algorithm, using variable subsets
 841 of (A) $D_{n,m}$ and (B) initial $S_{k,m}$ spectra. In (A), the root-mean-square deviations between the
 842 predicted and measured $\text{Fe}^{3+}/\text{Fe}^{\text{TOT}}$ for the entire dataset, $\text{RMSD } \text{Fe}^{3+}/\text{Fe}^{\text{TOT}}$, is represented as
 843 a function of the mean and range of the $\text{Fe}^{3+}/\text{Fe}^{\text{TOT}}$ values of the subset of data. In (B), it is
 844 represented as a function the mean and difference of $\text{Fe}^{3+}/\text{Fe}^{\text{TOT}}$ of the two initial S spectra. .
 845 Black points show where calculations were made; lines and colors were obtained by
 846 triangular interpolation.
 847



848
 849
 850
 851
 852

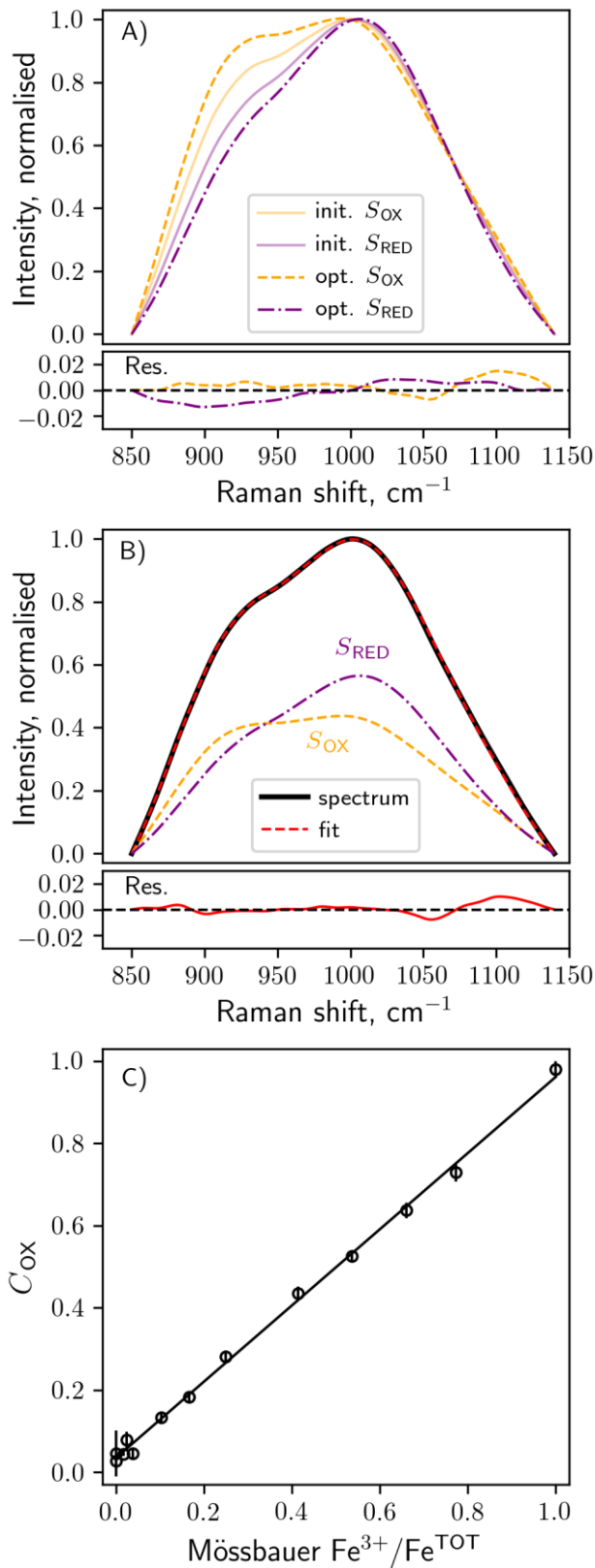


Figure 6: Results of the *ALS MCR* algorithm using the entire $D_{n,m}$ dataset, with initial (init.) $S_{k,m}$ spectra at $\text{Fe}^{3+}/\text{Fe}^{\text{TOT}} = 0.66$ and 0.25 . A) Init. and optimised (opt.) oxidised (S_{OX}) and reduced (S_{RED}) endmember spectra; residuals between the optimised S_{OX} and S_{RED} components and the means of spectra recorded for samples with $\text{Fe}^{3+}/\text{Fe}^{\text{TOT}} = 0$ and 1 are shown in the bottom panel. B) Comparison of the mean spectrum at $\text{Fe}^{3+}/\text{Fe}^{\text{TOT}} = 0.41$ (black line) and its fit (dotted red line) obtained by mixing the S_{OX} and S_{RED} endmembers; residual shown in the bottom panel. C) The fraction of the oxidised end-member, C_{OX} , against the $\text{Fe}^{3+}/\text{Fe}^{\text{TOT}}$ values determined by Mössbauer spectroscopy for the MORB glass standards. The line is a linear fit to the data. If not visible, errors are smaller than the symbols.

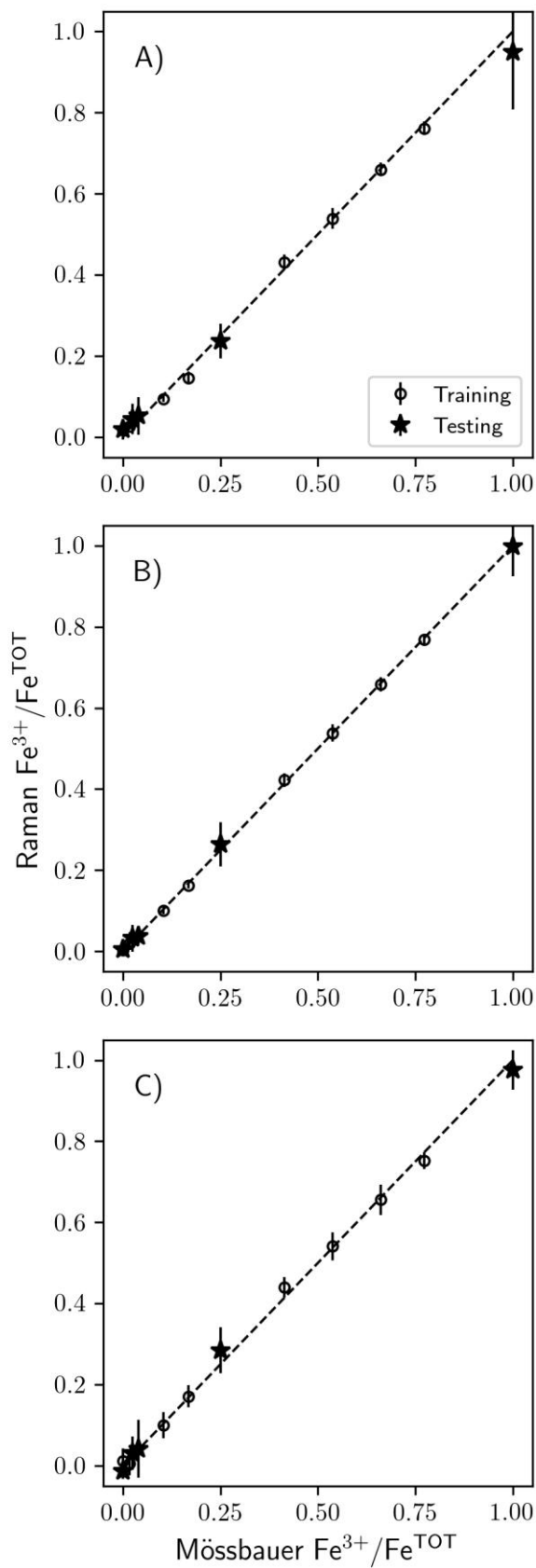
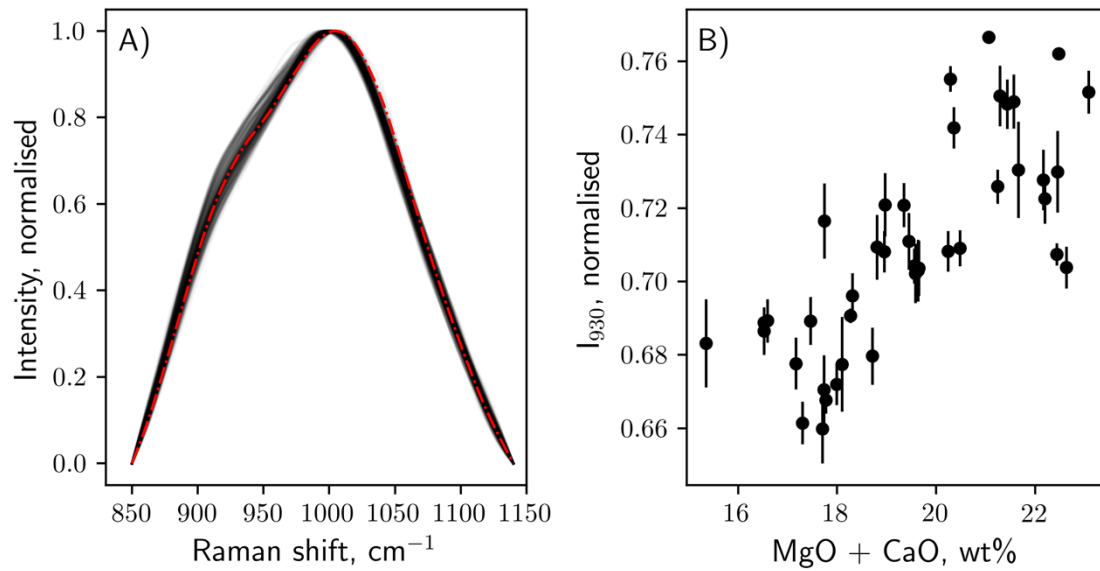


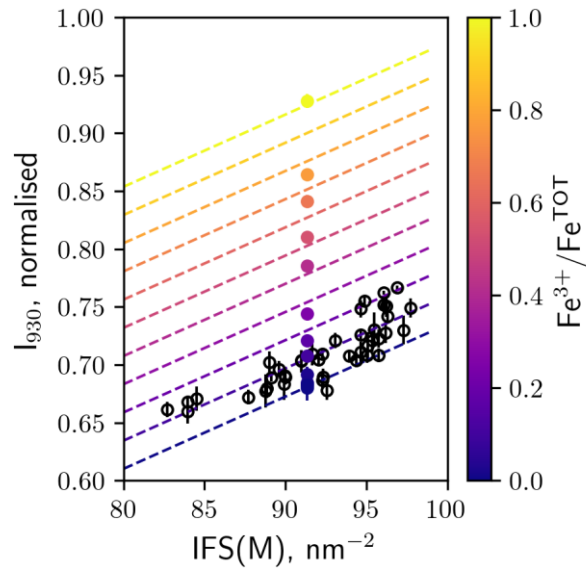
Figure 7: Raman $\text{Fe}^{3+}/\text{Fe}^{\text{TOT}}$ against Mössbauer $\text{Fe}^{3+}/\text{Fe}^{\text{TOT}}$ values for the MORB glass standards. Raman values were obtained from the A) *Kernel Ridge*, B) *Support Vector*, and C) *Neural Network* algorithms. See Table 1 for root-mean-square deviations of each dataset. If not visible, errors are smaller than the symbols.

914 **Figure 8:** A) Normalised baseline-subtracted Raman spectra of 42 natural MORB glasses
915 (see Table S1). The red dotted line is the spectrum of the glass standard with $\text{Fe}^{3+}/\text{Fe}^{\text{TOT}} =$
916 0.10(1). B) I_{930} as a function of the concentration (wt%) of MgO + CaO in the glasses.
917



918
919

920 **Figure 9:** I_{930} as a function of the mean ionic field strength of modifier cations, IFS(M) for
921 natural MORB glasses (open symbols) and MORB standards (solid symbols). Dotted lines
922 represent the values of the model (eq. 7, see text) that links I_{930} to IFS(M) and $\text{Fe}^{3+}/\text{Fe}^{\text{TOT}}$ in
923 MORB glasses. The colors reflect the $\text{Fe}^{3+}/\text{Fe}^{\text{TOT}}$ ratio (see colorbar).
924



925

926

927 **Figure 10:** Neural network predicted versus measured composition of natural MORB
 928 glasses. The standard deviations between the measured and predicted values for each subset
 929 are given for each compositional component.

